

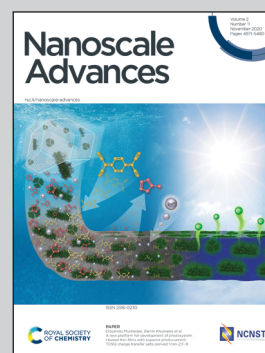


Showcasing research from Professor Guang Zhu's laboratory, Key Laboratory of Spin Electron and Nanomaterials of Anhui Higher Education Institutes, Suzhou University, Suzhou 234000, P. R. China.

A carbon-coated shuttle-like  $\text{Fe}_2\text{O}_3/\text{Fe}_{1-x}\text{S}$  heterostructure derived from metal-organic frameworks with high pseudocapacitance for ultrafast lithium storage

Carbon-coated  $\text{Fe}_2\text{O}_3/\text{Fe}_{1-x}\text{S}$  heterostructure is synthesized by annealing Fe-based metal-organic frameworks and sublimed sulfur as precursors. When evaluated as anode material for lithium ions batteries (LIBs), it exhibits excellent lithium ions storage performance and outstanding cycling stability at very high current density. The extraordinary performances for lithium ions storage can be attributed to its high electrical conductivity and enhanced pseudocapacitive contribution from surface effects. The current strategy is promising to synthesize the carbon-coated heterostructure derived from metal-organic frameworks for next-generation energy-storage application.

As featured in:



See Guang Zhu, Haifeng Xu *et al.*, *Nanoscale Adv.*, 2020, 2, 5201.

Cite this: *Nanoscale Adv.*, 2020, 2, 5201

# A carbon-coated shuttle-like Fe<sub>2</sub>O<sub>3</sub>/Fe<sub>1-x</sub>S heterostructure derived from metal–organic frameworks with high pseudocapacitance for ultrafast lithium storage†

Guang Zhu,<sup>id</sup>\*<sup>a</sup> Xiaojie Zhang,<sup>bc</sup> Yanjiang Li,<sup>a</sup> Guangzhen Zhao,<sup>id</sup><sup>a</sup> Haifeng Xu<sup>\*a</sup> and Zhong Jin<sup>id</sup><sup>d</sup>

Pursuing active, low-cost, and stable electrode materials with superior rate capability and long-life cycling performances for lithium-ion batteries remains a big challenge. In this study, a carbon-coated shuttle-like Fe<sub>2</sub>O<sub>3</sub>/Fe<sub>1-x</sub>S heterostructure is synthesized by simply annealing Fe-based metal–organic frameworks (MIL-88(Fe)) as precursors and sublimed sulfur. Carbon-coated Fe<sub>2</sub>O<sub>3</sub>/Fe<sub>1-x</sub>S displays a unique structure with ultrafine Fe<sub>2</sub>O<sub>3</sub>/Fe<sub>1-x</sub>S nanoparticles distributed in the hollow and porous carbon matrix, which offers a large specific surface area and fast charge transfer ability, and alleviates the volume change upon cycling. When evaluated as an anode material for lithium-ion batteries, it exhibits an ultra-high specific capacity of 1200 mA h g<sup>-1</sup> at 0.1 A g<sup>-1</sup>, and superior high rate capability with a capacity of 345 mA h g<sup>-1</sup> at a very high current density of 5.0 A g<sup>-1</sup> owing to its high electrical conductivity and enhanced pseudocapacitive contribution from surface effects. The current strategy is promising to synthesize the carbon-coated porous structure from metal–organic frameworks for next-generation energy-storage applications.

Received 7th May 2020

Accepted 18th July 2020

DOI: 10.1039/d0na00372g

rsc.li/nanoscale-advances

## 1. Introduction

During the past few years, lithium-ion batteries (LIBs) have occupied a dominant position in portable electronic devices, including mobile phones, electric transport, and minor medical facilities. However, owing to the low theoretical capacity (372 mA h g<sup>-1</sup>) and limited rate capability of the current commercial graphite anode, LIBs are unable to meet the ever-increasing demands of power and energy density for high-performance electric vehicles and large-scale energy storage systems.<sup>1–6</sup> Thus, the major obstacle of LIBs presented to scientists is to explore the novel and high-performance electrode materials with excellent ability for fast discharging/charging as well as long cycling life.<sup>7,8</sup> To date, iron-based

metal sulfides and oxides have attracted intensive attention as anode materials due to their high capacities, extensive resources, low cost, and environmental benignity. Unfortunately, Fe<sub>2</sub>O<sub>3</sub> usually suffers from an undesirable large volume expansion, resulting in a dramatic capacity fading during cycling.<sup>9,10</sup> In addition, the inherent poor electrical conductivity of Fe<sub>2</sub>O<sub>3</sub> hinders its rate performance, particularly at high current densities.<sup>11–13</sup> Therefore, it is urgent to explore novel Fe<sub>2</sub>O<sub>3</sub>-based electrode materials with high capacity, long cycling stability, and excellent rate capability.

In order to overcome the volume change and improve the rate capability of Fe<sub>2</sub>O<sub>3</sub>-based electrode materials, numerous promising strategies have been developed.<sup>14,15</sup> One efficient method is to fabricate nanostructured materials combined with a carbonaceous matrix with high electrical conductivity. In general, nanoscale Fe<sub>2</sub>O<sub>3</sub> can effectively reduce Li<sup>+</sup> diffusion distance and increase the contact area between active materials and electrolyte, thus leading to a high capacity. Moreover, carbon-coated Fe<sub>2</sub>O<sub>3</sub> nanocomposites can not only inherit the advantages of nanostructured Fe<sub>2</sub>O<sub>3</sub> (large contact area, abundant active reaction sites, short diffusion path, and strain accommodation) but also significantly improve the electrical conductivity of Fe<sub>2</sub>O<sub>3</sub> and act as a buffer to alleviate the volume changes and reduce the agglomeration of nanoparticles during cycling, which allows the high rate capability and cycling stability. Although some efforts have been made to prepare

<sup>a</sup>Key Laboratory of Spin Electron and Nanomaterials of Anhui Higher Education Institutes, Suzhou University, Suzhou 234000, P. R. China. E-mail: guangzhu@ahsztc.edu.cn; Xuhaifeng@ahszu.edu.cn

<sup>b</sup>National & Local Joint Engineering Research Center for Mineral Salt Deep Utilization, Key Laboratory for Palygorskite Science and Applied Technology of Jiangsu Province, Huaiyin Institute of Technology, Huaian 223003, China

<sup>c</sup>School of Electrical and Power Engineering, China University of Mining and Technology, Xuzhou, 221116, China

<sup>d</sup>Key Laboratory of Mesoscopic Chemistry of MOE, Jiangsu Key Laboratory of Advanced Organic Materials, School of Chemistry and Chemical Engineering, Nanjing University, Nanjing 210023, China

† Electronic supplementary information (ESI) available. See DOI: 10.1039/d0na00372g





carbon-coated  $\text{Fe}_2\text{O}_3$  nanocomposites with enhanced electrochemical performance, great challenges are still remaining, including the avoidance of toxic precursors and rigorous conditions.<sup>16</sup> Therefore, it is very necessary to develop a facile approach with low cost and high efficiency to fabricate carbon-coated  $\text{Fe}_2\text{O}_3$  nanocomposites. Recently, metal-organic framework (MOF)-derived carbon-coated nanostructure composites have exhibited promising applications in LIBs.<sup>17–19</sup> Benefiting from the advantages of improved electrical conductivity and mechanical flexibility of the carbon layer, the hybrid electrodes exhibit high reversible capacity, long cycle life, and excellent rate performance.<sup>20,21</sup> Recently, capacitive charge storage is considered to be beneficial for high-rate charging/discharging.<sup>22</sup> In particular, pseudocapacitance arises from the fast faradaic charge-transfer reactions occurring at the electrode surface and near-surface contacted with the electrolyte, which can induce fast ion transfer rate and high power density.<sup>23–26</sup> Thus, enhancing the pseudocapacitive contribution of electrode materials should be an effective strategy to realize high-rate capability.

In this study, shuttle-like hollow and porous  $\text{Fe}_2\text{O}_3/\text{Fe}_{1-x}\text{S}@C$  hybrid structure was fabricated using MIL-88(Fe) as a precursor. In this unique structure, ultra-small  $\text{Fe}_2\text{O}_3/\text{Fe}_{1-x}\text{S}$  nanocrystals can shorten the ion diffusion distance and facilitate the charge transfer, while the carbon layer serves as a conductive matrix, which alleviates the stress associated with the large volume expansion upon cycling, suppresses the agglomeration of nanoparticles, and enhances the electrical conductivity of the composite during the charge/discharge process. When evaluated as an anode for LIBs, the  $\text{Fe}_2\text{O}_3/\text{Fe}_{1-x}\text{S}@C$  electrode exhibits a high specific capacity of  $1200 \text{ mA h g}^{-1}$  at  $0.1 \text{ A g}^{-1}$  with an excellent rate capability of  $345 \text{ mA h g}^{-1}$  at a high current density of  $5.0 \text{ A g}^{-1}$ . Such remarkable electrochemical performance of the  $\text{Fe}_2\text{O}_3/\text{Fe}_{1-x}\text{S}@C$  hybrid should be mainly ascribed to the unique microstructure inherited from the precursor and the significant pseudocapacitive contribution, accelerating the mass transport and facilitating the charge transfer upon cycling.

## 2. Experimental

MIL-88(Fe) was prepared *via* a facile hydrothermal method according to a previous study.<sup>27</sup> In a typical procedure, 1.35 g of  $\text{FeCl}_3 \cdot 6\text{H}_2\text{O}$  (5 mmol) and 0.58 g of fumaric acid (5 mmol) were dissolved into 50 ml of deionized water, respectively. Then, the above two solutions were mixed and stirred for 30 min, and the suspension was transferred into a round-bottomed flask and kept at  $100 \text{ }^\circ\text{C}$  for 4 h in an oil-bath. After the reaction mixture is naturally cooled to room temperature, a reddish-brown product was collected and washed with deionized water and ethanol several times.

First, the as-synthesized MIL-88(Fe) was carbonized at  $600 \text{ }^\circ\text{C}$  for 2 h at a heating rate of  $2 \text{ }^\circ\text{C min}^{-1}$  under  $\text{N}_2$  atmosphere. The product was proved to be  $\text{Fe}_3\text{O}_4@C$  with trace metal Fe (denoted as  $\text{Fe}_3\text{O}_4/\text{Fe}@C$ ).<sup>28,29</sup> Second, for the oxidation experiment, the  $\text{Fe}_3\text{O}_4/\text{Fe}@C$  composite was heated to  $300 \text{ }^\circ\text{C}$  in a quartz tube under air atmosphere for 1 h at a heating rate of  $2 \text{ }^\circ\text{C min}^{-1}$  and the final product  $\text{Fe}_2\text{O}_3@C$  was obtained.

The obtained MIL-88(Fe) was mixed with sublimed sulfur (1 : 1, w/w) by grinding and subsequently carbonized at  $600 \text{ }^\circ\text{C}$  at a heating rate of  $2 \text{ }^\circ\text{C min}^{-1}$  in a nitrogen atmosphere for 2 h to obtain  $\text{Fe}_2\text{O}_3/\text{Fe}_{1-x}\text{S}@C$ . The characterizations and electrochemical tests of  $\text{Fe}_2\text{O}_3@C$  and  $\text{Fe}_2\text{O}_3/\text{Fe}_{1-x}\text{S}@C$  samples can be referred to the ESI.<sup>†</sup>

## 3. Results and discussion

The FESEM image and XRD pattern of as-prepared MIL-88 (Fe) are presented in Fig. S1 and S2 (ESI<sup>†</sup>). As expected, MIL-88(Fe) exhibits a shuttle-like structure with a smooth surface and size of  $\sim 3 \text{ } \mu\text{m}$  in length, and its XRD pattern is consistent with the previous report.<sup>27</sup> The XRD patterns of  $\text{Fe}_2\text{O}_3@C$  and  $\text{Fe}_2\text{O}_3/\text{Fe}_{1-x}\text{S}@C$  (Fig. 1a and b) can be well indexed to the cubic maghemite  $\text{Fe}_2\text{O}_3$  phase (JCPDS card no. 39-1346) and the hexagonal pyrrhotite  $\text{Fe}_{1-x}\text{S}$  phase (JCPDS card no. 22-1120), respectively. In addition, a broad diffraction peak located at around  $24^\circ$  is attributed to the amorphous carbon coated on the surface of the nanoparticles.<sup>30,31</sup> From the SEM images of  $\text{Fe}_2\text{O}_3@C$  and  $\text{Fe}_2\text{O}_3/\text{Fe}_{1-x}\text{S}@C$  (as shown in Fig. 2a and c), it can be clearly seen that the products can maintain the original shuttle-like shape of the precursor, and the magnified FESEM images (Fig. 2b and d) show that the surfaces of  $\text{Fe}_2\text{O}_3@C$  and  $\text{Fe}_2\text{O}_3/\text{Fe}_{1-x}\text{S}@C$  are composed of numerous nanoparticles. The elemental mapping measured *via* energy dispersive spectroscopy (EDS) confirms the co-existence of Fe, O, and C elements in  $\text{Fe}_2\text{O}_3@C$ , as shown in Fig. S3 (ESI<sup>†</sup>). Apart from Fe, O, and C, S element is also observed in the EDS mapping of  $\text{Fe}_2\text{O}_3/\text{Fe}_{1-x}\text{S}@C$ , as shown in Fig. S4 (ESI<sup>†</sup>). In addition, the element contents of  $\text{Fe}_2\text{O}_3@C$  and  $\text{Fe}_2\text{O}_3/\text{Fe}_{1-x}\text{S}@C$  are listed in Table S1 (ESI<sup>†</sup>). The Fe contents are almost the same in both samples. Notably, the carbon content in  $\text{Fe}_2\text{O}_3/\text{Fe}_{1-x}\text{S}@C$  is slightly higher than that in  $\text{Fe}_2\text{O}_3@C$ , and the probable reason is that the sublimated sulfur consumes more oxide element, thus resulting in the relative higher carbon content.

The transmission electron microscope (TEM) image of  $\text{Fe}_2\text{O}_3@C$  in Fig. 3a shows that  $\text{Fe}_2\text{O}_3$  nanoparticles with sizes ranging from 20 to 100 nm are uniformly distributed in the amorphous carbon matrix. Besides, the magnified TEM image (Fig. 3b) displays the thickness of the amorphous carbon layer to be about 3–5 nm, which exhibits a highly ordered lattice fringe with a spacing of  $2.5 \text{ \AA}$ , corresponding to the (311) plane of  $\text{Fe}_2\text{O}_3$ . Similarly, as shown in Fig. 3c and d, the size of  $\text{Fe}_2\text{O}_3/$

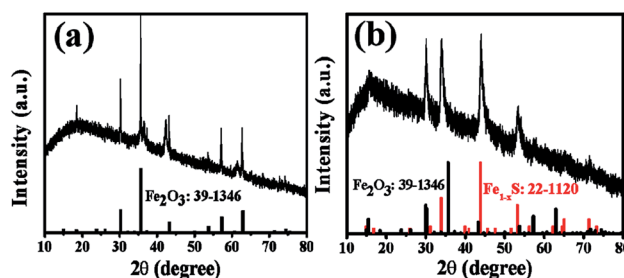


Fig. 1 XRD patterns of (a)  $\text{Fe}_2\text{O}_3@C$  and (b)  $\text{Fe}_2\text{O}_3/\text{Fe}_{1-x}\text{S}@C$ .



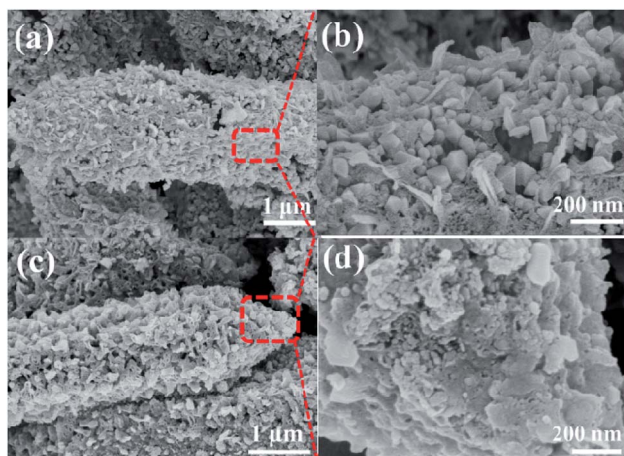


Fig. 2 FESEM images at low and high-magnification of (a and b)  $\text{Fe}_2\text{O}_3@\text{C}$  and (c and d)  $\text{Fe}_2\text{O}_3/\text{Fe}_{1-x}\text{S}@\text{C}$ .

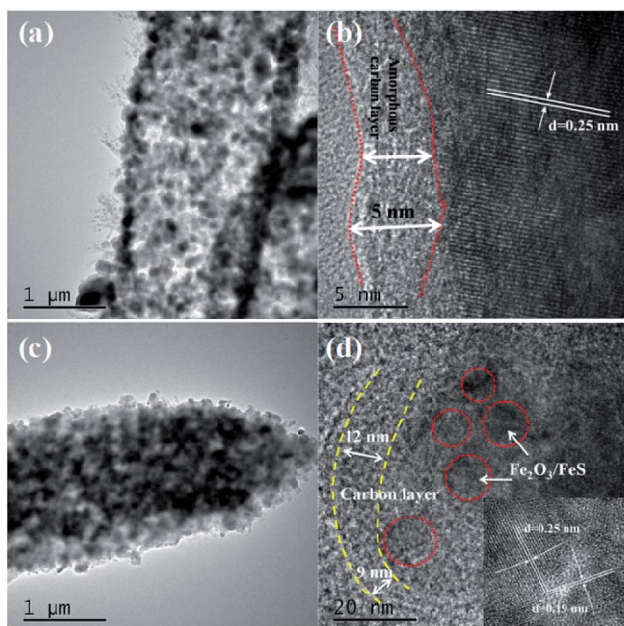


Fig. 3 TEM images at different magnifications of (a and b)  $\text{Fe}_2\text{O}_3@\text{C}$  and (c and d)  $\text{Fe}_2\text{O}_3/\text{Fe}_{1-x}\text{S}@\text{C}$ .

$\text{Fe}_{1-x}\text{S}$  nanoparticles is about 10–50 nm, and the thickness of the amorphous carbon layer is about 8 nm. Moreover, the magnified TEM image of  $\text{Fe}_2\text{O}_3/\text{Fe}_{1-x}\text{S}@\text{C}$  in Fig. 3d shows the clear lattice fringes of  $\text{Fe}_2\text{O}_3$  with a spacing of 2.5 Å and  $\text{Fe}_{1-x}\text{S}$  with a spacing of 1.9 Å, corresponding to the (311) plane of  $\text{Fe}_2\text{O}_3$  and the (220) plane of  $\text{Fe}_{1-x}\text{S}$ .

The specific surface areas and corresponding pore size distributions of  $\text{Fe}_2\text{O}_3@\text{C}$  and  $\text{Fe}_2\text{O}_3/\text{Fe}_{1-x}\text{S}@\text{C}$  were further studied by nitrogen adsorption–desorption isotherms based on the Brunauer–Emmett–Teller (BET) method, and the results are shown in Fig. 4a and b.  $\text{Fe}_2\text{O}_3@\text{C}$  exhibits a typical IV isotherm along with an obvious H1 hysteresis, which shows the feature of the mesoporous structure. However, the  $\text{Fe}_2\text{O}_3/\text{Fe}_{1-x}\text{S}@\text{C}$  shows

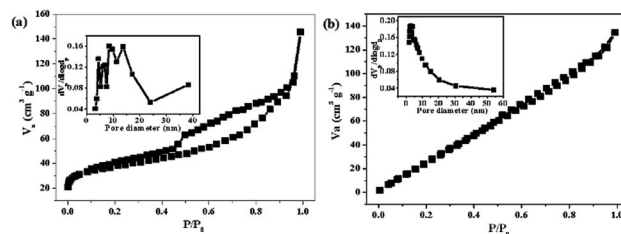


Fig. 4  $\text{N}_2$  adsorption/desorption isotherms of (a)  $\text{Fe}_2\text{O}_3@\text{C}$  and (b)  $\text{Fe}_2\text{O}_3/\text{Fe}_{1-x}\text{S}@\text{C}$ . Inset is the corresponding pore size distributions.

a typical III isotherm, implying the co-existence of microporous and mesoporous structures in the samples.<sup>32,33</sup> The corresponding pore size distributions are shown in the inset of Fig. 4a and b. It can be found that the pores in  $\text{Fe}_2\text{O}_3@\text{C}$  are mainly distributed in the range of mesopores, whereas a hierarchically porous structure with micro/mesopores exists in  $\text{Fe}_2\text{O}_3/\text{Fe}_{1-x}\text{S}@\text{C}$ . Notably, the difference between  $\text{Fe}_2\text{O}_3/\text{Fe}_{1-x}\text{S}@\text{C}$  and  $\text{Fe}_2\text{O}_3@\text{C}$  on  $\text{N}_2$  adsorption/desorption isotherms and pore size distributions should be ascribed to the sulfidation process, creating micropores in the resultant  $\text{Fe}_2\text{O}_3/\text{Fe}_{1-x}\text{S}@\text{C}$ , which contributes to its high specific surface area. Particularly, the specific surface area of  $\text{Fe}_2\text{O}_3/\text{Fe}_{1-x}\text{S}@\text{C}$  is  $183.4 \text{ m}^2 \text{ g}^{-1}$ , which is larger than that of  $\text{Fe}_2\text{O}_3@\text{C}$  ( $133.5 \text{ m}^2 \text{ g}^{-1}$ ). Apparently, the large specific surface area could supply a good contact between electrode materials and electrolyte, and the hierarchically mesoporous and microporous structure will be beneficial to accommodate the volume changes, resulting in the superior stability and fast  $\text{Li}^+$  diffusion. The existence of carbon materials in  $\text{Fe}_2\text{O}_3@\text{C}$  and  $\text{Fe}_2\text{O}_3/\text{Fe}_{1-x}\text{S}@\text{C}$  composites are confirmed by Raman spectroscopy, as shown in Fig. 5. Two main peaks located at around  $1340 \text{ cm}^{-1}$  and  $1580 \text{ cm}^{-1}$  are assigned to D (disordered carbon or defective graphitic structure) and G (graphitic carbon) bands, respectively. The peak intensity ratio of the D band/G band ( $I_D/I_G$ ) characterizes the degree of disorder or defects in the carbon structure in the samples.<sup>34</sup> The values of  $I_D/I_G$  for  $\text{Fe}_2\text{O}_3@\text{C}$  and  $\text{Fe}_2\text{O}_3/\text{Fe}_{1-x}\text{S}@\text{C}$  composites are calculated to be 0.94 and 0.96, respectively,

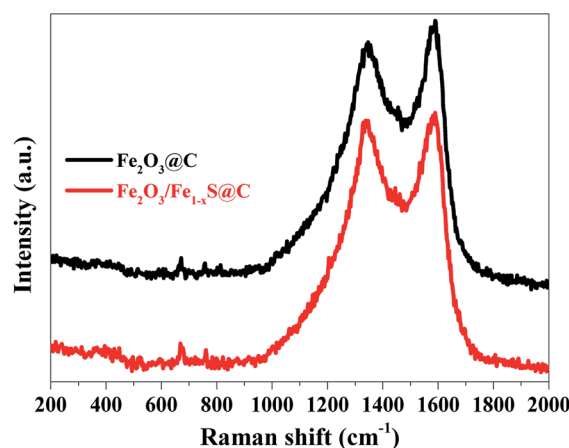


Fig. 5 Raman spectra of  $\text{Fe}_2\text{O}_3@\text{C}$  and  $\text{Fe}_2\text{O}_3/\text{Fe}_{1-x}\text{S}@\text{C}$  composites.



indicating the co-existence of both amorphous and graphitic carbon.<sup>35,36</sup> The other weak peaks located at about 380, 400, 680, and 750  $\text{cm}^{-1}$  represent Fe–O and Fe–S Raman modes. Moreover, the absence of two characteristic peaks (214 and 280  $\text{cm}^{-1}$  corresponding to  $A_{1g}$  and  $E_g$ ) of  $\text{Fe}_2\text{O}_3$  in the Raman spectra of  $\text{Fe}_2\text{O}_3@\text{C}$  and  $\text{Fe}_2\text{O}_3/\text{Fe}_{1-x}\text{S}@\text{C}$  should be attributed to the phonon confinement effect in which the  $\text{Fe}_2\text{O}_3$  signal is blocked by the carbon in  $\text{Fe}_2\text{O}_3@\text{C}$  and  $\text{Fe}_2\text{O}_3/\text{Fe}_{1-x}\text{S}@\text{C}$  composites.<sup>37–39</sup>

The electrochemical impedance spectra (EIS) of  $\text{Fe}_2\text{O}_3@\text{C}$  and  $\text{Fe}_2\text{O}_3/\text{Fe}_{1-x}\text{S}@\text{C}$  electrodes were measured in the frequency range from 0.1 Hz to 100 kHz after 100 charge/discharge cycles, and the results are shown in Fig. 6a and b. The equivalent circuit model shown in the inset of Fig. 6a was used to fit and analyze the Nyquist plots. In general, the Nyquist plots are composed of an indistinct depressed semicircle in a high frequency related to the resistance from the solid electrolyte interface layer ( $R_f$ ), an obvious large semicircle in the middle frequency region representing the charge-transfer resistance ( $R_{ct}$ ), and an inclined line in low frequency region corresponding to the Warburg diffusion resistance ( $Z_w$ ). The fitted  $R_{ct}$  values for  $\text{Fe}_2\text{O}_3@\text{C}$  and  $\text{Fe}_2\text{O}_3/\text{Fe}_{1-x}\text{S}@\text{C}$  electrodes are about 503 and 118  $\Omega$ , respectively, indicating the enhanced charge transfer of the  $\text{Fe}_2\text{O}_3/\text{Fe}_{1-x}\text{S}$  heterostructure. The reduced  $R_{ct}$  will increase the electron transfer kinetics and subsequently improve the rate capability of the  $\text{Fe}_2\text{O}_3/\text{Fe}_{1-x}\text{S}@\text{C}$  electrode. Moreover, the  $\text{Fe}_2\text{O}_3/\text{Fe}_{1-x}\text{S}@\text{C}$  electrode exhibits a more vertically inclined line than that of  $\text{Fe}_2\text{O}_3@\text{C}$ , showing its significant capacitive contribution behavior, which results in a fast charging–discharging rate.<sup>40,41</sup>

Fig. 7a and b show the initial four CV curves of  $\text{Fe}_2\text{O}_3@\text{C}$  and  $\text{Fe}_2\text{O}_3/\text{Fe}_{1-x}\text{S}@\text{C}$  electrodes between 0.005 and 3.0 V at a scan rate of 0.2  $\text{mV s}^{-1}$ , respectively. The irreversible broad and sharp cathodic peak at around 0.6 V for the  $\text{Fe}_2\text{O}_3@\text{C}$  electrode as well as a minor peak at 1.1 V and a broad peak centered at 0.6 V for the  $\text{Fe}_2\text{O}_3/\text{Fe}_{1-x}\text{S}@\text{C}$  electrode in the first cathodic scan can be ascribed to the decomposition of the electrolyte with the formation of the solid electrolyte interface film and the reduction of  $\text{Fe}_2\text{O}_3$  and  $\text{Fe}_{1-x}\text{S}$  to form metallic Fe and amorphous  $\text{Li}_2\text{O}$ .<sup>42,43</sup> The related electrochemical reactions can be described as follows:

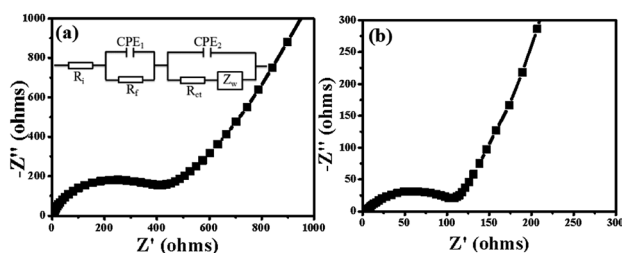
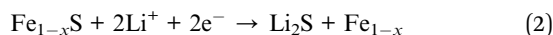
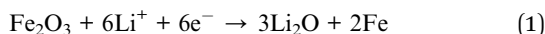


Fig. 6 EIS plots of (a)  $\text{Fe}_2\text{O}_3@\text{C}$  and (b)  $\text{Fe}_2\text{O}_3/\text{Fe}_{1-x}\text{S}@\text{C}$  electrodes after 100 cycles, and inset of (a) is the equivalent circuit model.

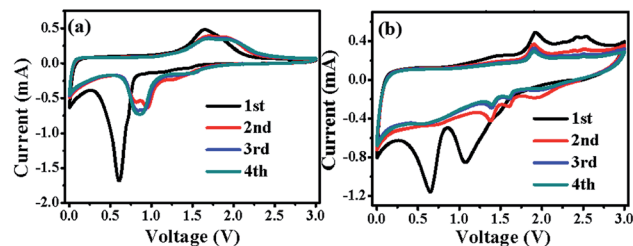
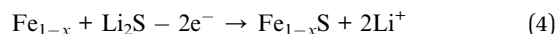
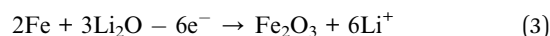


Fig. 7 Initial four CV curves of (a)  $\text{Fe}_2\text{O}_3@\text{C}$  and (b)  $\text{Fe}_2\text{O}_3/\text{Fe}_{1-x}\text{S}@\text{C}$  electrodes.

From the second cycle, the cathodic peaks of both electrodes particularly the  $\text{Fe}_2\text{O}_3/\text{Fe}_{1-x}\text{S}@\text{C}$  electrode move to a higher potential, which is related to the structural change of metal oxides and sulfides caused by first lithiation/de-lithiation.<sup>44</sup> A higher potential favors  $\text{Li}^+$  insertion in electrode materials, leading to better electrochemical performance.<sup>45</sup> For the first anodic sweep, there are two peaks at 1.6 and 1.8 V for the  $\text{Fe}_2\text{O}_3@\text{C}$  electrode, and 1.7 and 2.3 V for  $\text{Fe}_2\text{O}_3/\text{Fe}_{1-x}\text{S}@\text{C}$ , indicating the oxidation of metallic Fe to  $\text{Fe}_2\text{O}_3$  and  $\text{Fe}_{1-x}\text{S}$  via a multistep oxidation process.<sup>46,47</sup> The corresponding electrochemical reaction can be summarized as follows:



The CV peaks almost overlapped with each other after the second cycle, indicating their superior electrochemical stability.

Fig. 8a and b compare the cycle stabilities of  $\text{Fe}_2\text{O}_3@\text{C}$  and  $\text{Fe}_2\text{O}_3/\text{Fe}_{1-x}\text{S}@\text{C}$  electrodes at a current density of 0.1  $\text{A g}^{-1}$  for 100 cycles. The cycling stability of the  $\text{Fe}_2\text{O}_3@\text{C}$  electrode is attenuated slightly in the first 40 cycles, and the capacity keeps at 786  $\text{mA h g}^{-1}$  after 100 cycles, whereas the capacity of the  $\text{Fe}_2\text{O}_3/\text{Fe}_{1-x}\text{S}@\text{C}$  electrode decays in the first 10 cycles, and then shows an obvious increase in the subsequent cycles, implying its excellent cycling stability. The reversible capacity of the  $\text{Fe}_2\text{O}_3/\text{Fe}_{1-x}\text{S}@\text{C}$  electrode can be maintained at 1200  $\text{mA h g}^{-1}$  with an approximately 99% capacity retention owing to the synergistic effects of  $\text{Fe}_2\text{O}_3$  and  $\text{Fe}_{1-x}\text{S}$ , which is much higher than that of the  $\text{Fe}_2\text{O}_3@\text{C}$  electrode. The  $\text{Fe}_2\text{O}_3/\text{Fe}_{1-x}\text{S}@\text{C}$  electrode after 100 cycles was measured via FESEM (Fig. S5, ESI<sup>†</sup>), and no obvious change can be detected after cycling, indicating the excellent stability of the electrode materials. Furthermore, the rate performances of  $\text{Fe}_2\text{O}_3@\text{C}$  and  $\text{Fe}_2\text{O}_3/\text{Fe}_{1-x}\text{S}@\text{C}$  electrodes were also evaluated at different current densities ranging from 0.1, 0.2, 0.5, 1.0, 2.0, and 5.0  $\text{A g}^{-1}$ , and the results are shown in Fig. 8c and d. The corresponding reversible specific capacities of  $\text{Fe}_2\text{O}_3@\text{C}$  ( $\text{Fe}_2\text{O}_3/\text{Fe}_{1-x}\text{S}@\text{C}$ ) are about 880.5 (1139.7), 761.1 (1047), 644.5 (875.6), 511.2 (735.3), 358.9 (546.1) and 140 (345)  $\text{mAh g}^{-1}$ . When the current density returns to 0.1  $\text{A g}^{-1}$ , the reversible capacities can be recovered to 900 (1189.2)  $\text{mAh g}^{-1}$ , showing the excellent rate capability.<sup>48</sup> In addition, the lithium storage performance of the  $\text{Fe}_2\text{O}_3/\text{Fe}_{1-x}\text{S}@\text{C}$  electrode at a current density of 10  $\text{A g}^{-1}$  was also tested, and the results are shown in Fig. S6 (ESI<sup>†</sup>). Even





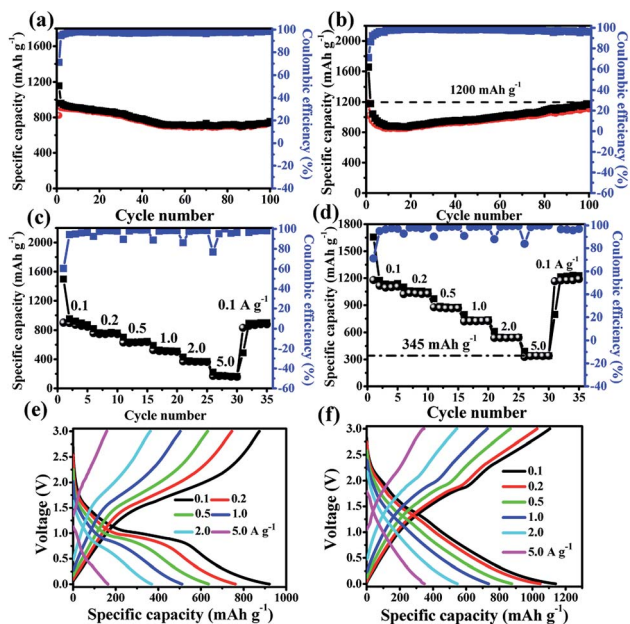


Fig. 8 Cycling stability at  $0.1 \text{ A g}^{-1}$  for 100 cycles, rate performance and corresponding galvanostatic charge–discharge curves at numerous current densities (from  $0.1$  to  $5.0 \text{ A g}^{-1}$ ) of (a, c and e)  $\text{Fe}_2\text{O}_3@C$  and (b, d and f)  $\text{Fe}_2\text{O}_3/\text{Fe}_{1-x}\text{S}@C$  electrodes.

though at such a high current density, the capacity can still be maintained at  $98 \text{ mA h g}^{-1}$ . The main reason should be ascribed to the unique structure and the carbon matrix, which can facilitate the transport of  $\text{Li}^+$  and electrons, thus leading to excellent rate capability. Fig. 8e and f display the corresponding charge/discharge curves at each current density for  $\text{Fe}_2\text{O}_3@C$  and  $\text{Fe}_2\text{O}_3/\text{Fe}_{1-x}\text{S}@C$  electrodes, respectively. It can be seen that the  $\text{Fe}_2\text{O}_3/\text{Fe}_{1-x}\text{S}@C$  electrode shows less polarization at high current densities than  $\text{Fe}_2\text{O}_3@C$ . More importantly, it is obvious that the capacities of the  $\text{Fe}_2\text{O}_3/\text{Fe}_{1-x}\text{S}@C$  electrode at each current density are greatly higher than those of  $\text{Fe}_2\text{O}_3@C$  electrode, particularly at a high current density of  $5.0 \text{ A g}^{-1}$ . In addition, we compared the performance of the  $\text{Fe}_2\text{O}_3/\text{Fe}_{1-x}\text{S}@C$  in this study with other Fe-based electrodes reported in previous literatures (Table S2, ESI†). The results show that the  $\text{Fe}_2\text{O}_3/\text{Fe}_{1-x}\text{S}@C$  exhibits the highest specific capacity and excellent rate capability. The outstanding electrochemical performance of the  $\text{Fe}_2\text{O}_3/\text{Fe}_{1-x}\text{S}@C$  electrode can be ascribed to (i) the excellent charge transfer ability due to the introduction of  $\text{Fe}_{1-x}\text{S}$  and the formation of the heterostructure between  $\text{Fe}_2\text{O}_3$  and  $\text{Fe}_{1-x}\text{S}$ ; (ii) the short ion-diffusion pathways due to the ultra-small nanoparticles; (iii) the excellent structural stability ensured by the carbon buffer and porous structure.

It is well known that there are two typical types of energy storage behaviors in LIBs: redox pseudocapacitive process taking place on the surface of the electrode materials, and the diffusion-controlled process in the bulk of the electrode materials. In order to further study the fast reaction kinetics of different electrode materials, according to the Trasatti analysis reported by Dunn *et al.*, CV tests at various sweep rates from  $0.2$  to  $1.4 \text{ mV s}^{-1}$  were carried out, which can quantify and calculate

the contribution percentage from the pseudocapacitive effect and diffusion-controlled  $\text{Li}^+$  insertion process.<sup>24,49</sup> As shown in Fig. 9a and b, all peak current intensity ( $i$ ) increase with the increase in the scan rate ( $\nu$ ), and their relationship follow the equation:  $i = a\nu^b$ ,<sup>50</sup> where  $a$  and  $b$  both are adjustable values. When the value of  $b$  is  $0.5$ , the ionic diffusion is dominant, whereas when  $b = 1$ , the reaction is mostly pseudocapacitive behavior controlled. According to previous literature,<sup>23,51</sup> the  $b$  value can be calculated from the slope of the fitted line based on  $\log(i)$  versus  $\log(\nu)$  plots, and the fitted results are shown in Fig. 9c and d for  $\text{Fe}_2\text{O}_3@C$  and  $\text{Fe}_2\text{O}_3/\text{Fe}_{1-x}\text{S}@C$  electrodes, respectively. The  $b$  values for the selected peak 1 and peak 2 of the  $\text{Fe}_2\text{O}_3@C$  electrode are  $0.69$  and  $0.78$ , respectively, which are lower than those of the  $\text{Fe}_2\text{O}_3/\text{Fe}_{1-x}\text{S}@C$  electrode (peak 1,  $0.79$ ; peak 2,  $0.85$ ), indicating the higher pseudocapacitive contribution of the  $\text{Fe}_2\text{O}_3/\text{Fe}_{1-x}\text{S}@C$  electrode than that of  $\text{Fe}_2\text{O}_3@C$ . In addition, the total current intensity can be divided into two parts according to the following eqn (5):<sup>52,53</sup>

$$i = k_1\nu + k_2\nu^{1/2} \quad (5)$$

where  $i$  is the total current intensity. The values of  $k_1\nu$  and  $k_2\nu^{1/2}$  represent the potentials controlled by the pseudocapacitive effect and ionic diffusion-controlled process, respectively. Therefore, we calculated the pseudocapacitive contribution by determining  $k_1$  and  $k_2$  values, and the results are displayed in Fig. 9e and f. For the  $\text{Fe}_2\text{O}_3@C$  electrode, the pseudocapacitive contributions are  $31\%$ ,  $31.7\%$ ,  $34.7\%$ ,  $37.3\%$ ,  $40.5\%$ ,  $46.5\%$ , and  $51.5\%$  at the scan rates of  $0.2$ ,  $0.4$ ,  $0.6$ ,  $0.8$ ,  $1.0$ ,  $1.2$  and

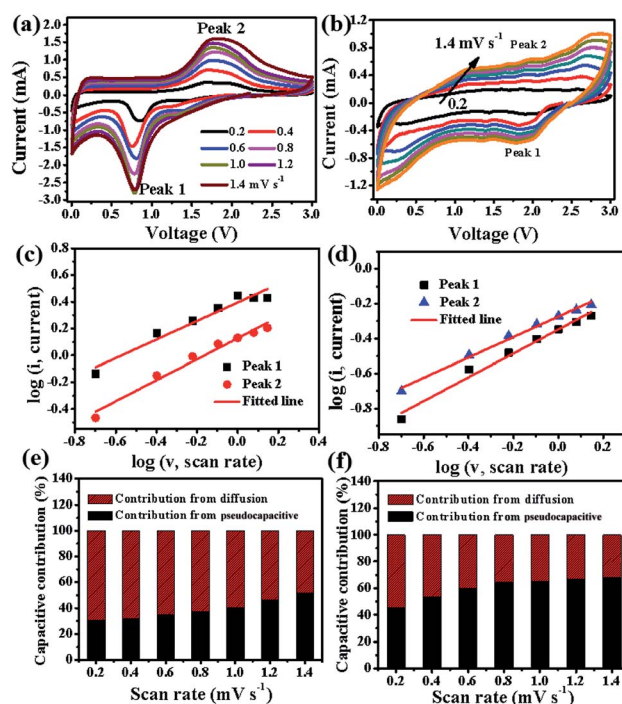


Fig. 9 CV curves at various scan rates in the range from  $0.2$  to  $1.4 \text{ mV s}^{-1}$ , fitted lines based  $\log(\nu)$  versus  $\log(i)$  for selected peak 1 and peak 2, capacitive contribution percentages at different scan rates for (a, c and e)  $\text{Fe}_2\text{O}_3@C$  and (b, d and f)  $\text{Fe}_2\text{O}_3/\text{Fe}_{1-x}\text{S}@C$  electrodes.



1.4 mV s<sup>-1</sup>, respectively, showing an enhancement with the increase in the scan rate. The contributions are 45.1%, 53.3%, 59.9%, 64.6%, 65%, 67.1% and 68.1% for the Fe<sub>2</sub>O<sub>3</sub>/Fe<sub>1-x</sub>S@C electrode, much higher than those of the Fe<sub>2</sub>O<sub>3</sub>@C electrode at same scan rates. The improved capacitive contribution of the Fe<sub>2</sub>O<sub>3</sub>/Fe<sub>1-x</sub>S@C electrode can be attributed to the Fe<sub>2</sub>O<sub>3</sub> and Fe<sub>1-x</sub>S heterostructure, which can offer more active reaction sites and decrease electrode polarization, leading to fast Li<sup>+</sup> insertion/extraction and enhanced Li<sup>+</sup> storage performance.<sup>48,54</sup> The tiny Fe<sub>2</sub>O<sub>3</sub>/Fe<sub>1-x</sub>S nanocrystals could not only offer an abundant interface and reactive sites but also enhance the transfer rate of lithium ions, resulting in an improved rate capability. Moreover, the coated carbon layer serves as a conductive matrix, which relieves the stress associated with the large volume change, suppresses the agglomeration of the nanoparticles and also improves the electrical conductivity of the composite during the charge/discharge process.

## 4. Conclusions

In conclusion, an effective approach, to design the Fe<sub>2</sub>O<sub>3</sub>/Fe<sub>1-x</sub>S heterostructure coated by an amorphous carbon layer *via* annealing MOFs and sublimed sulfur, was developed. When evaluated as the anode material for LIBs, Fe<sub>2</sub>O<sub>3</sub>/Fe<sub>1-x</sub>S@C features more excellent Li<sup>+</sup> storage performance (1200 mA h g<sup>-1</sup> at 0.1 A g<sup>-1</sup> after 100 cycles) and outstanding rate capability (345 mA h g<sup>-1</sup> at 5.0 A g<sup>-1</sup>) as compared with Fe<sub>2</sub>O<sub>3</sub>@C. The improvement in the Li<sup>+</sup> diffusion capability and charge-transfer ability is mainly responsible for the extraordinary performance of the Fe<sub>2</sub>O<sub>3</sub>/Fe<sub>1-x</sub>S@C electrode. The sulfidation strategy developed in this study should be a promising way to prepare other carbon-coated metal oxide/sulfide heterostructures from MOFs with high capacity and superior rate for LIBs.

## Conflicts of interest

There are no conflicts to declare.

## Acknowledgements

This work is supported by the Provincial Natural Science Foundation of Anhui (1908085ME120), Primary Research and Development Program of Anhui Province (201904a05020087), Doctoral Fund of Ministry of Education of China (No. 2018M642356), Innovative Research Team of Anhui Provincial Education Department (2016SCXPTTD), Natural Science Project of the Jiangsu Higher Education Institutions (19KJB480001, 18KJA430006), National & Local Joint Engineering Research Center for Deep Utilization Technology of Rock-salt Resource (SF201802, SF201803), Key Discipline of Material Science and Engineering of Suzhou University (2017XJZDXK3).

## Notes and references

1 B. Kang and G. Ceder, Battery materials for ultrafast charging and discharging, *Nature*, 2009, **458**, 190–193.

- X. Zhang, G. Zhu, M. Wang, J. Li, T. Lu and L. Pan, Covalent-organic-frameworks derived N-doped porous carbon materials as anode for superior long-life cycling lithium and sodium ion batteries, *Carbon*, 2017, **116**, 686–694.
- C. Yingying, G. Kaiming, G. Hongbo, A. Huixiang, P. Jie, L. Yayuan, C. Xueqin, Z. Junwei and G. Hongwei, Metal-Oleate Complex Derived Bimetallic Oxides Nanoparticles Encapsulated in 3D Graphene Networks as Anodes for Efficient Lithium Storage with Pseudocapacitance, *Nano-Micro Lett.*, 2019, **11**, 15.
- S. Yu, V. M. Hong Ng, F. Wang, Z. Xiao, C. Li, L. B. Kong, W. Que and K. Zhou, Synthesis and application of iron-based nanomaterials as anodes of lithium-ion batteries and supercapacitors, *J. Mater. Chem. A*, 2018, **6**, 9332–9367.
- L. Kong, M. Zhong, W. Shuang, Y. Xu and X.-H. Bu, Electrochemically active sites inside crystalline porous materials for energy storage and conversion, *Chem. Soc. Rev.*, 2020, **49**, 2378–2407.
- S. Zheng, X. Li, B. Yan, Q. Hu, Y. Xu, X. Xiao, H. Xue and H. Pang, Transition-metal (Fe, Co, Ni) based metal-organic frameworks for electrochemical energy storage, *Adv. Energy Mater.*, 2017, **7**, 1602733.
- D. Pan, N. Wan, Y. Ren, W. Zhang, X. Lu, Y. Wang, Y. S. Hu and Y. Bai, Enhanced structural and electrochemical stability of self-similar rice-shaped SnO<sub>2</sub> nanoparticles, *ACS Appl. Mater. Interfaces*, 2017, **9**, 9747–9755.
- D. Wang, T. Xu, Y. Li, D. Pan, X. Lu, Y. S. Hu, S. Dai and Y. Bai, Integrated surface functionalization of Li-rich cathode materials for Li-ion batteries, *ACS Appl. Mater. Interfaces*, 2018, **10**, 41802–41813.
- M. Zhang, E. Liu, T. Cao, H. Wang, C. Shi, J. Li, C. He, F. He, L. Ma and N. Zhao, Sandwiched graphene inserted with graphene-encapsulated yolk-shell γ-Fe<sub>2</sub>O<sub>3</sub> nanoparticles for efficient lithium ion storage, *J. Mater. Chem. A*, 2017, **5**, 7035–7042.
- X. Zhang, M. Wang, G. Zhu, D. Li, D. Yan, T. Lu and L. Pan, Porous cake-like TiO<sub>2</sub> derived from metal-organic frameworks as superior anode material for sodium ion batteries, *Ceram. Int.*, 2017, **43**, 2398–2402.
- Y. Yang, W. Yuan, X. Zhang, C. Wang, Y. Yuan, Y. Huang, Y. Ye, Z. Qiu and Y. Tang, A review on Fe<sub>x</sub>O<sub>y</sub>-based materials for advanced lithium-ion batteries, *Renewable Sustainable Energy Rev.*, 2020, **127**, 109884.
- T. Jiang, F. Bu, X. Feng, I. Shakir, G. Hao and Y. Xu, Porous Fe<sub>2</sub>O<sub>3</sub> nanoframeworks encapsulated within three-dimensional graphene as high-performance flexible anode for lithium-ion battery, *ACS Nano*, 2017, **11**, 5140–5147.
- B. Sun, S. Lou, Z. Qian, P. Zuo, C. Du, Y. Ma, H. Huo, J. Xie, J. Wang and G. Yin, Pseudocapacitive Li<sup>+</sup> storage boosts ultrahigh rate performance of structure-tailored CoFe<sub>2</sub>O<sub>4</sub>@Fe<sub>2</sub>O<sub>3</sub> hollow spheres triggered by engineered surface and near-surface reactions, *Nano Energy*, 2019, **66**, 104179.
- X. Lv, J. Deng, B. Wang, J. Zhong, T. K. Sham and X. Sun, γ-Fe<sub>2</sub>O<sub>3</sub>@CNTs anode materials for lithium ion batteries investigated by electron energy loss spectroscopy, *Chem. Mater.*, 2017, **29**, 3499–3506.



- 15 K. Lee, S. Shin, T. Degen, W. Lee and Y. S. Yoon, In situ analysis of SnO<sub>2</sub>/Fe<sub>2</sub>O<sub>3</sub>/RGO to unravel the structural collapse mechanism and enhanced electrical conductivity for lithium-ion batteries, *Nano Energy*, 2017, **32**, 397–407.
- 16 N. F. W. Thissen, M. A. Verheijen, R. G. Houben, C. van der Marel, W. M. M. Kessels and A. A. Bol, Synthesis of single-walled carbon nanotubes from atomic-layer-deposited Co<sub>3</sub>O<sub>4</sub> and Co<sub>3</sub>O<sub>4</sub>/Fe<sub>2</sub>O<sub>3</sub> catalyst films, *Carbon*, 2017, **121**, 389–398.
- 17 F. Zheng, M. He, Y. Yang and Q. Chen, Nano electrochemical reactors of Fe<sub>2</sub>O<sub>3</sub> nanoparticles embedded in shells of nitrogen-doped hollow carbon spheres as high-performance anodes for lithium-ion batteries, *Nanoscale*, 2015, **7**, 3410–3417.
- 18 S. L. Zhang, B. Y. Guan, H. B. Wu and X. W. Lou, Metal-organic framework-assisted synthesis of compact Fe<sub>2</sub>O<sub>3</sub> nanotubes in Co<sub>3</sub>O<sub>4</sub> host with enhanced lithium storage properties, *Nano-Micro Lett.*, 2018, **10**, 44.
- 19 X. Zhang, X. Gao, Z. Wu, M. Zhu, Q. Jiang, S. Zhou, K. Hong and Z. Rao, Effects of binders on electrochemical sodium storage performance with porous CoFe<sub>2</sub>O<sub>4</sub> nanocubes derived from metal-organic frameworks, *Chem. Phys.*, 2019, **523**, 124–129.
- 20 X. Zhang, W. Qin, D. Li, D. Yan, B. Hu, Z. Sun and L. Pan, Metal-organic framework derived porous CuO/Cu<sub>2</sub>O composite hollow octahedrons as high performance anode materials for sodium ion batteries, *Chem. Commun.*, 2015, **51**, 16413–16416.
- 21 Z. Xiu, M. H. Alfaruqi, J. Gim, J. Song, S. Kim, T. V. Thi, P. T. Duong, J. P. Baboo, V. Mathew and J. Kim, Hierarchical porous anatase TiO<sub>2</sub> derived from a titanium metal-organic framework as a superior anode material for lithium ion batteries, *Chem. Commun.*, 2015, **51**, 12274–12277.
- 22 E. F. Rodriguez, F. Xia, D. Chen, A. F. Hollenkamp and R. A. Caruso, N-doped Li<sub>4</sub>Ti<sub>5</sub>O<sub>12</sub> nanoflakes derived from 2D protonated titanate for high performing anodes in lithium ion batteries, *J. Mater. Chem. A*, 2016, **4**, 7772–7780.
- 23 V. Augustyn, P. Simon and B. Dunn, Pseudocapacitive oxide materials for high-rate electrochemical energy storage, *Energy Environ. Sci.*, 2014, **7**, 1597–1614.
- 24 V. Augustyn, J. Come, M. A. Lowe, J. W. Kim, P.-L. Taberna, S. H. Tolbert, H. D. Abruña, P. Simon and B. Dunn, High-rate electrochemical energy storage through Li<sup>+</sup> intercalation pseudocapacitance, *Nat. Mater.*, 2013, **12**, 518.
- 25 P. Simon, Y. Gogotsi and B. Dunn, Where do batteries end and supercapacitors begin?, *Science*, 2014, **343**, 1210–1211.
- 26 Z. Tong, H. Xu, G. Liu, J. Zhao and Y. Li, Pseudocapacitive effect and Li<sup>+</sup> diffusion coefficient in three-dimensionally ordered macroporous vanadium oxide for energy storage, *Electrochem. Commun.*, 2016, **69**, 46–49.
- 27 X. Xu, J. Li, M. Wang, Y. Liu, T. Lu and L. Pan, Shuttle-like porous carbon rods from carbonized metal-organic frameworks for high-performance capacitive deionization, *ChemElectroChem*, 2016, **3**, 993–998.
- 28 X. Zhang, W. Ou-Yang, G. Zhu, T. Lu and L. Pan, Shuttle-like carbon-coated FeP derived from metal-organic frameworks for lithium-ion batteries with superior rate capability and long-life cycling performance, *Carbon*, 2019, **143**, 116–124.
- 29 L. Wang, Y. Zhang, X. Li, Y. Xie, J. He, J. Yu and Y. Song, The MIL-88A-derived Fe<sub>3</sub>O<sub>4</sub>-carbon hierarchical nanocomposites for electrochemical sensing, *Sci. Rep.*, 2015, **5**, 14341.
- 30 S. Surblé, C. Serre, C. Mellot-Draznieks, F. Millange and G. Férey, A new isoreticular class of metal-organic-frameworks with the MIL-88 topology, *Chem. Commun.*, 2006, 284–286.
- 31 Y. Jia, Y. Wang, L. Dong, J. Huang, Y. Zhang, J. Su and J. Zang, A hybrid of titanium nitride and nitrogen-doped amorphous carbon supported on SiC as a noble metal-free electrocatalyst for oxygen reduction reaction, *Chem. Commun.*, 2015, **51**, 2625–2628.
- 32 X. Liu, T. Chen, H. Chu, L. Niu, Z. Sun, L. Pan and C. Q. Sun, Fe<sub>2</sub>O<sub>3</sub>-reduced graphene oxide composites synthesized via microwave-assisted method for sodium ion batteries, *Electrochim. Acta*, 2015, **166**, 12–16.
- 33 X. Zhang, G. Zhu, D. Yan, T. Lu and L. Pan, MnO@C nanorods derived from metal-organic frameworks as anode for superiorly stable and long-life sodium-ion batteries, *J. Alloys Compd.*, 2017, **710**, 575–580.
- 34 J. Li, J. Li, D. Yan, S. Hou, X. Xu, T. Lu, Y. Yao, W. Mai and L. Pan, Design of pomegranate-like clusters with NiS<sub>2</sub> nanoparticles anchored on nitrogen-doped porous carbon for improved sodium ion storage performance, *J. Mater. Chem. A*, 2018, **6**, 6595–6605.
- 35 N. Zheng, G. Jiang, X. Chen, J. Mao, N. Jiang and Y. Li, Battery separators functionalized with edge-rich MoS<sub>2</sub>/C hollow microspheres for the uniform deposition of Li<sub>2</sub>S in high-performance lithium-sulfur batteries, *Nano-Micro Lett.*, 2019, **11**, 43.
- 36 M. Gockeln, S. Pokhrel, F. Meierhofer, J. Glenneberg, M. Schowalter, A. Rosenauer, U. Fritsching, M. Busse, L. Mädler and R. Kun, Fabrication and performance of Li<sub>4</sub>Ti<sub>5</sub>O<sub>12</sub>/C Li-ion battery electrodes using combined double flame spray pyrolysis and pressure-based lamination technique, *J. Power Sources*, 2018, **374**, 97–106.
- 37 Y. Huang, M. Zheng, Z. Lin, B. Zhao, S. Zhang, J. Yang, C. Zhu, H. Zhang, D. Sun and Y. Shi, Flexible cathodes and multifunctional interlayers based on carbonized bacterial cellulose for high-performance lithium-sulfur batteries, *J. Mater. Chem. A*, 2015, **3**, 10910–10918.
- 38 Y. Fang, L. Xiao, X. Ai, Y. Cao and H. Yang, Hierarchical carbon framework wrapped Na<sub>3</sub>V<sub>2</sub>(PO<sub>4</sub>)<sub>3</sub> as a superior high-rate and extended lifespan cathode for sodium-ion batteries, *Adv. Mater.*, 2015, **27**, 5895–5900.
- 39 J. Qian, M. Zhou, Y. Cao, X. Ai and H. Yang, Template-free hydrothermal synthesis of nanoembossed mesoporous LiFePO<sub>4</sub> microspheres for high-performance lithium-ion batteries, *J. Phys. Chem. C*, 2010, **114**, 3477–3482.
- 40 Y. Wang, C. Wang, Y. Wang, H. Liu and Z. Huang, Superior sodium-ion storage performance of Co<sub>3</sub>O<sub>4</sub>@nitrogen-doped carbon: derived from a metal-organic framework, *J. Mater. Chem. A*, 2016, **4**, 5428–5435.
- 41 J. Wang, J. Polleux, J. Lim and B. Dunn, Pseudocapacitive contributions to electrochemical energy storage in TiO<sub>2</sub>





- (anatase) nanoparticles, *J. Phys. Chem. C*, 2007, **111**, 14925–14931.
- 42 J. Qu, Y. X. Yin, Y. Q. Wang, Y. Yan, Y. G. Guo and W. G. Song, Layer structured  $\alpha$ -Fe<sub>2</sub>O<sub>3</sub> nanodisk/reduced graphene oxide composites as high-performance anode materials for lithium-ion batteries, *ACS Appl. Mater. Interfaces*, 2013, **5**, 3932–3936.
- 43 C. Zhao, X. Shao, Y. Zhang and X. Qian, Fe<sub>2</sub>O<sub>3</sub>/reduced graphene oxide/Fe<sub>3</sub>O<sub>4</sub> composite in situ grown on Fe foil for high-performance supercapacitors, *ACS Appl. Mater. Interfaces*, 2016, **8**, 30133–30142.
- 44 J. Shao, J. Zhang, J. Jiang, G. Zhou and M. Qu,  $\alpha$ -Fe<sub>2</sub>O<sub>3</sub>@CNSs nanocomposites as superior anode materials for lithium-ion batteries, *Electrochim. Acta*, 2011, **56**, 7005–7011.
- 45 M. Gao, P. Zhou, P. Wang, J. Wang, C. Liang, J. Zhang and Y. Liu, Fe<sub>2</sub>O<sub>3</sub>/C anode materials of high capacity and cycle stability for lithium-ion batteries synthesized by carbothermal reduction, *J. Alloys Compd.*, 2013, **565**, 97–103.
- 46 B. Wu, H. Song, J. Zhou and X. Chen, Iron sulfide-embedded carbon microsphere anode material with high-rate performance for lithium-ion batteries, *Chem. Commun.*, 2011, **47**, 8653–8655.
- 47 Y. Xu, W. Li, F. Zhang, X. Zhang, W. Zhang, C. S. Lee and Y. Tang, In situ incorporation of FeS nanoparticles/carbon nanosheets composite with an interconnected porous structure as a high-performance anode for lithium ion batteries, *J. Mater. Chem. A*, 2016, **4**, 3697–3703.
- 48 Z. Li, Z. Xu, X. Tan, H. Wang, C. M. B. Holt, T. Stephenson, B. C. Olsen and D. Mitlin, Mesoporous nitrogen-rich carbons derived from protein for ultra-high capacity battery anodes and supercapacitors, *Energy Environ. Sci.*, 2013, **6**, 871–878.
- 49 T. Brezesinski, J. Wang, S. H. Tolbert and B. Dunn, Ordered mesoporous  $\alpha$ -MoO<sub>3</sub> with iso-oriented nanocrystalline walls for thin-film pseudocapacitors, *Nat. Mater.*, 2010, **9**, 146.
- 50 J. B. Cook, H. S. Kim, Y. Yan, J. S. Ko, S. Robbennolt, B. Dunn and S. H. Tolbert, Mesoporous MoS<sub>2</sub> as a transition metal dichalcogenide exhibiting pseudocapacitive Li and Na-ion charge storage, *Adv. Energy Mater.*, 2016, **6**, 1501937.
- 51 H. Liu, Z. Bi, X. G. Sun, R. R. Unocic, M. P. Paranthaman, S. Dai and G. M. Brown, Mesoporous TiO<sub>2</sub>-B microspheres with superior rate performance for lithium ion batteries, *Adv. Mater.*, 2011, **23**, 3450–3454.
- 52 H. Kim, M. G. Kim and J. Cho, Unique structural changes of three-dimensionally ordered macroporous TiO<sub>2</sub> electrode materials during electrochemical cycling, *Adv. Energy Mater.*, 2012, **2**, 1425–1432.
- 53 H. X. Dang, Y. M. Lin, K. C. Klavetter, T. H. Cell, A. Heller and C. B. Mullins, Lithium insertion/deinsertion characteristics of nanostructured amorphous tantalum oxide thin films, *ChemElectroChem*, 2014, **1**, 158–164.
- 54 L. Zhang, K. Zhao, Y. Luo, Y. Dong, W. Xu, M. Yan, W. Ren, L. Zhou, L. Qu and L. Mai, Acetylene black induced heterogeneous growth of macroporous CoV<sub>2</sub>O<sub>6</sub> nanosheet for high-rate pseudocapacitive lithium-ion battery anode, *ACS Appl. Mater. Interfaces*, 2016, **8**, 7139–7146.

